HHS Public Access

Author manuscript

ACS Appl Mater Interfaces. Author manuscript; available in PMC 2022 April 07.

Published in final edited form as:

ACS Appl Mater Interfaces. 2021 April 07; 13(13): 14974–14984. doi:10.1021/acsami.1c00993.

Gold Nanorod–Melanin Hybrids for Enhanced and Prolonged Photoacoustic Imaging in the Near-Infrared-II Window

Wonjun Yim[#],
Materials Science and Engineering Program, University of California San Diego, La Jolla, California 92093, United States

Jiajing Zhou[#],
Department of Nanoengineering, University of California San Diego, La Jolla, California 92093, United States

Yash Mantri,
Department of Bioengineering, University of California San Diego, La Jolla, California 92093, United States

Matthew N. Creyer,
Department of Nanoengineering, University of California San Diego, La Jolla, California 92093, United States

Colman A. Moore,
Department of Nanoengineering, University of California San Diego, La Jolla, California 92093, United States

Jesse V. Jokerst
Materials Science and Engineering Program, University of California San Diego, La Jolla, California 92093, United States; Department of Bioengineering and Department of Radiology, University of California San Diego, La Jolla, California 92093, United States

[#] These authors contributed equally to this work.

Abstract

Photoacoustic (PA) imaging holds great promise as a noninvasive imaging modality. Gold nanorods (GNRs) with absorption in the second near-infrared (NIR-II) window have emerged as excellent PA probes because of their tunable optical absorption, surface modifiability, and low toxicity. However, pristine GNRs often undergo shape transition upon laser illumination due to

Corresponding Author: Jesse V. Jokerst – jjokerst@ucsd.edu.

The authors declare no competing financial interest.

ASSOCIATED CONTENT

Supporting Information

The Supporting Information is available free of charge at https://pubs.acs.org/doi/10.1021/acsami.1c00993.

Mushroom and brush conformation, SEM images, stability test of GNR@PDA, material information of GNR@PDA150, ICP-MS data, absorption cross-sectional area of GNR and GNR@PDAs, PA images and optical extinction of GNR and GNR@PDA50 at the elevated concentration, TEM images of shape transition of GNR and GNR@PDAs, changes in UV–vis–NIR absorption spectra of GNR and GNR@PDAs before and after 5 min of laser illumination, TEM images of shape transition of GNR@PDAs, TEM images of PDA capsules, PDA-coated gold nanospheres, and detailed information of eq 3 (PDF)

Complete contact information is available at: https://pubs.acs.org/10.1021/acsami.1c00993

thermodynamic instability, leading to a reduced PA signal after a few seconds of imaging. Here, we report monodisperse GNR–melanin nanohybrids where a tunable polydopamine (PDA) coating was conformally coated on GNRs. GNR@PDAs showed a threefold higher PA signal than pristine GNRs due to the increased optical absorption, cross-sectional area, and thermal confinement. More importantly, the PA signal of GNR@PDAs only decreased by 29% during the 5 min of laser illumination in the NIR-II window, while significant attenuation (77%) was observed for GNRs. The GNR@PDAs maintained 87% of its original PA signal *in vivo* even after 10 min of laser illumination. This PDA-enabled strategy affords a rational design for robust PA imaging probes and provides more opportunities for other types of photomediated biomedicines, such as photothermal and photodynamic regimens.

Graphical Abstract

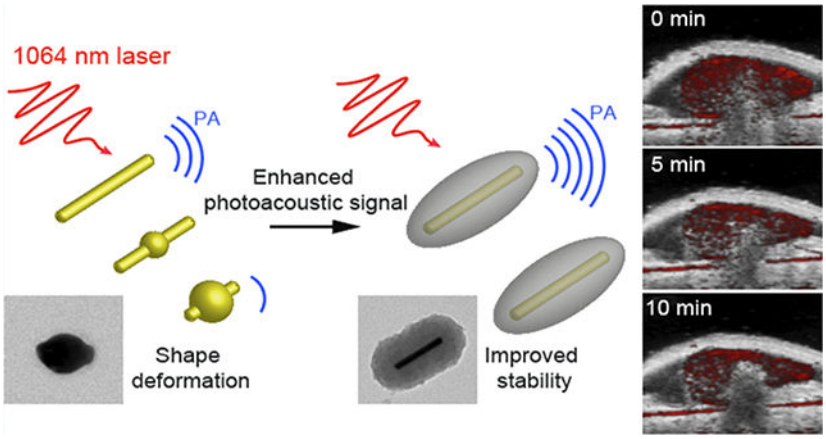

Keywords

gold nanorods; melanin; photoacoustic imaging; polydopamine coating; second near-infrared window

INTRODUCTION

Photoacoustic (PA) imaging is a light in/sound out approach and holds great promise as a noninvasive imaging modality for biomolecular sensing and disease diagnosis.[1–3] It has improved penetration depth and spatiotemporal resolution versus pure optical approaches.[4–6] PA imaging can use endogenous or exogenous contrast media; a myriad of such exogenous contrast agents have been reported such as small-molecule NIR dyes[7] and metallic[8] and organic[9] nanoparticles. These have been engineered to image cells, tissues, and biological processes of interest.[10] Plasmonic metallic nanoparticles are particularly popular because of their facile surface modification, tunable localized surface plasmonic resonance (LSPR), high photothermal efficiency, and relatively inert biological activity in the human body.[11–14] However, extensive light–tissue interactions (*e.g.*, scattering and absorbance) can attenuate the input light and impair the PA imaging, thus leading to limited penetration depth and decreased imaging sensitivity.[4]

Gold nanorods (GNRs) have recently attracted immense attention to address this challenge for improving the imaging depth and sensitivity.[15–18] Specifically, GNRs with a high aspect ratio can absorb photons in the second near-infrared (NIR-II) window (1000–1700 nm) where biological tissues have lower background absorption.[19–22] The NIR-II window thus offers deeper light penetration and higher maximum permission exposure versus the visible spectral and NIR-I (650–900 nm) range.[23–25] One limitation of the GNRs is their anisotropic structure that is susceptible to deformation after laser illumination. GNRs are easily deformed upon NIR-I and NIR-II laser irradiation because of their thermodynamic instability: it is found that the high-pulsed laser induces the creation of point and line defects that grow into planar defects (*e.g.*, multiple twins and stacking faults) in the interior of GNRs.[26,27] These defects migrate gold atoms at {110} facets to the more stable {100} and {111} facets to minimize their surface energy.[27] Thus, the additional laser energy can cause the rod to deform into a sphere. In addition, melting of GNRs is also observed under laser illumination, converting the shape into a sphere.[27–29] Consequently, the absorbance in the infrared region decays over time (<1 min) as the absorption peak blue shifts. Thus, the PA signal also attenuates because of the strong correlation between absorption and the PA signal.[13] This problem limits the utility of GNRs in PA imaging. Solutions to this problem include coating the GNRs with a stabilizing layer such as silica and metal–organic frameworks.[30,31] In contrast to these methods, we report organic molecule-mediated formation of GNR–melanin hybrids (GNR@PDAs), which enables a protective polydopamine (PDA) layer on GNRs to improve the optical absorption and thermal confinement.

Melanin is a natural pigment with multiple roles in biology such as photoprotection, metal ion chelation, and free radical scavenging.[32–35] Here, we used auto-oxidation of dopamine into PDA to successfully coat synthetic melanin on the surface of GNRs (Figure 1). PDA coating not only serves as a robust polymeric armor for the underlying GNRs but also exhibits a broadband absorption (400–1300 nm), suggesting that it may enhance the PA imaging while also protecting the underlying GNR.[36–38] Furthermore, it has been proved that PDA coating can serve as a biocompatible layer, reducing *in vivo* toxicity of the coated material.[39–41] No obvious toxicity or change in animal behavior was observed in our *in vivo* experiments; a detailed necroscopy will be performed in subsequent studies. Thus, we investigated PA efficiency of GNR@PDAs in both NIR-I (*e.g.*, 680 nm) and NIR-II (*e.g.*, 1064 nm) lasers versus bare GNRs. Moreover, we compared the time-dependent PA signal amplitude and optical extinction of GNR@PDAs with bare GNRs to verify the improved structural and thermal stability of the GNR@PDAs. Finally, we further removed the GNR core to make rod-shaped PDA capsules to investigate the function of the PDA shell during PA signal generation. This method is a versatile strategy to improve the photothermal efficiency and stability of nanoparticles for biomedical and environmental applications.[33]

EXPERIMENTAL SECTION

Materials.

Gold(III) chloride hydrate ($HAuCl_4$), hydroquinone, cetyltrimethylammonium bromide (CTAB), sodium borohydride ($NaBH_4$), silver nitrate ($AgNO_3$), dopamine hydrochloride,

bicine, *N,N*-dimethylformamide (DMF), copper(II) chloride dihydrate ($CuCl_2$), and mouse serum were purchased from Sigma-Aldrich (Atlanta, GA, USA). Methoxyl poly(ethylene glycol) (PEG) thiol (HS-mPEG, M_w 5k Da) was purchased from Nanocs. Dulbecco's modified Eagle's medium (DMEM) was purchased from Thermo Fisher. All reagents were used without further purification. Distilled water was used to make aqueous solutions. Transmission electron microscopy (TEM) grids were purchased from Ted Pella, Inc.

Methods.

Synthesis of GNR Particles.—We used a seed-mediated growth[42] for the synthesis of GNR particles with a high aspect ratio of 7.7 ± 3.3. Briefly, a seed solution was made by mixing an aqueous solution of 5 mL of CTAB (0.2 M) and 5 mL of $HAuCl_4$ (0.5 mM). Then, 600 μL of $NaBH_4$ (10 mM) was quickly injected to the seed solution under vigorous stirring at 1200 rpm. After 15 s of vigorous $NaBH_4$ reaction, the seed solution was incubated in a water bath at 30 °C for 1 h.

A growth solution was made by adding 10 mL of CTAB (0.2 M), 10 mL of $HAuCl_4$ (1.0 mM), and 120 μL of $AgNO_3$ (0.1 M), sequentially. Then, 650 μL of hydroquinone (0.1 M) was added under vigorous stirring at 1200 rpm. The color of the growth solution turned from yellow to transparent. Finally, 320 μL of the seed solution was injected to the growth solution under vigorous stirring at 1100 rpm. After 15 s of vigorous reaction, the solution was incubated in a water bath at 30 °C for 12 h before being purified with two centrifugation cycles at 7500*g* for 10 min.

Synthesis of PEGylated GNR Particles.—CTAB on the surface of GNRs was replaced by HS-mPEG *via* ligand exchange. The CTAB-stabilized GNR was dispersed in 2 mL of water and added to 4 mL of HS-mPEG (5 mg/mL in water, 1 mM) under vigorous stirring at 1000 rpm for 6 h. The resulting PEGylated GNRs were purified by centrifugation at 7500*g* for 10 min to remove the excess of HS-mPEG. The PEGylated GNRs were redispersed in water for future use.

Synthesis of PDA-Coated GNR Particles.—Typically, 200 μL of concentrated PEGylated GNRs was dispersed in 2 mL of bicine buffer (10 mM, pH 8.5) followed by 50, 100, 200, and 300 μL of dopamine solution (4 mg/mL in water) to make different coating thicknesses. The reaction solution was stirred at 1000 rpm for 12 h, and the resulting dark-brown product was purified by centrifugation at 7500*g* for 10 min. The GNR@PDAs were redispersed in water for future use.

Synthesis of Rod-Shaped PDA Capsules.—Typically, 100 μL of concentrated GNR@PDAs (0.5 μg/mL) in water was dispersed in 900 μL of the DMF solvent and centrifuged at 7500*g* for 10 min to exchange the solvent. Then, GNR@PDAs were redispersed in 900 μL of DMF, and 100 μL of $CuCl_2$ (50 mM) was added to remove the GNR core. The reaction solution was incubated at 60 °C for 6 h with generous stirring at 600 rpm before being purified with centrifugation at 6000*g* for 10 min.

Stability Test of PDA-Coated GNR Particles.—In brief, 50 μL of concentrated GNR@PDAs (0.05 μg/mL) was incubated in 100 μL of HCl (10 mM, pH ≈ 2), NaOH (10

mM, pH ≈ 12), NaCl (10 mM), and cell culture medium (DMEM) with 20, 10, or 5% of mouse serum, respectively for 1 h. Then, 100 μL of the sample was used for the dynamic light scattering (DLS) measurement.

In Vivo Subcutaneous Injection.—All animal experiments were performed in accordance with NIH guidelines and approved by the Institutional Animal Care and Use Committee (IACUC) under protocol S15050 at the University of California, San Diego. Matrigel was used to image the nanoparticle in a subcutaneous area of a murine model.[43] GNR@PDA (150 μL) in 50% of Matrigel was subcutaneously injected into the mice ($n = 3$) and imaged 10 min for testing PA signal stability. We used Matrigel only and uncoated gold nanorods as negative controls. All images were processed using Vevo LAB 3.1.0 software. Samples were imaged using a 40 MHz transducer.

Instrumentation.—TEM samples were examined *via* a JEOL JEM-1400 Plus operating at 80 kV. TEM images were taken using a Gatan 4k digital camera, and 10 μL of the samples was dropped onto the copper grids for TEM sample preparation. TEM images were processed using ImageJ software (Bethesda, MD, USA).[44] Scanning electron microscopy (SEM) samples were analyzed *via* FEI Apreo operating at a voltage of 10 kV and a current of 0.10 nA. 10 μL of the samples was dropped on the silicon wafer for sample preparation. Electron-dispersive X-ray spectroscopy (EDX) samples were examined using a Thermo Fisher Talos 200X transmission electron microscope operating at 200 kV. Scanning TEM images were acquired using Velox software, and the images were processed with Thermo Scientific software. The hydrodynamic diameter and ζ potential of the sample were calculated using a Malvern Instrument Zetasizer ZS 90. The sample (100 μL) was diluted in 900 μL of distilled water for the measurement. Ultraviolet–visible–NIR (UV–vis–NIR) absorption spectra of the sample were recorded using a PerkinElmer UV–vis–NIR spectrophotometer. Absorbance was read from 400 to 1380 nm with a step size of 2 nm. The inductively coupled plasma mass spectrometry (ICP-MS) analysis was conducted using a Thermo Scientific iCAP RQ ICP-MS in the Environmental and Complex Analysis Laboratory at UC San Diego. Samples were prepared and digested using 4% HNO_3 solution and *aqua regia* for the measurements. A VisualSonics Vevo 2100 LAZR imaging system was used to acquire PA imaging from 680 to 970 nm and 1064 nm. Samples were imaged using a 21 MHz-centered LZ 250 transducer. The peak energy is 45 ± 5 mJ at 20 Hz at the source. The specimens were aligned at a depth of 1 cm from the transducer. The laser was optimized and calibrated before the measurement.

Photothermal Conversion Efficiency of GNR and GNR@PDA.—Typically, 1 mL of GNR and GNR@PDA samples (O.D. ≈ 1) was placed in a quartz cuvette to measure the photothermal conversion efficiency. We used the 1064 nm laser, and the laser power was set up to 1.0 W/cm^2. Temperature was determined by an FLIR C5 camera. The recorded temperature was used to calculate the photothermal conversion efficiency.[38]

Data Analysis.—All PA data were processed using ImageJ software.[44] The raw image was converted to 8 bit images. The mean value and standard deviation of the PA intensity were then calculated based on the five regions of interest per tube. Statistical significance was

determined using GraphPad software. The statistical significance was calculated with the two-tailed PA intensity of GNR@PDA's *t*-test; *p*-values < 0.01 were considered to be significantly different.

RESULTS AND DISCUSSION

Synthesis and Characterization.

To obtain GNRs with LSPR in the NIR-II spectral range, we used a seed-mediated method[42] to prepare GNRs with dimensions of 95.07 ± 6.92 × 12.46 ± 1.36 nm (aspect ratio = 7.7) (Figure 2A and Table 1). The GNRs stabilized with CTAB had positively charged surfaces (45.47 ± 1.12 mV). Adding dopamine directly to CTAB-stabilized GNRs thus caused immediate aggregation because of the strong electrostatic interactions between negatively charged dopamine and positively charged GNRs. As a solution, we replaced CTAB with a methoxyl PEG thiol (HS-mPEG). The ζ potential of GNRs decreased to −10.2 ± 0.44 mV after ligand exchange, indicating successful conjugation of HS-mPEG. According to Flory–Huggins theory, polymer conformations attached to the interface can be described by the Flory radius ($F = n^{3/5}a$).[45] Here, n is the number of monomers per chain, and a is the monomer size (a = 3.5 Å for PEG).[45,46] Based on this theory, PEG chains can form either mushroom or brush conformations depending on the grafting density. For example, if the distance (D) between the attachment points of PEG to a surface of GNR is lower than F ($D < F$), then the PEG chains will form a mushroom conformation. They will form a brush conformation if the grafting density is high ($D > F$).[46] At a fixed concentration of CTAB-stabilized GNR (0.2 μg/mL), 1 mg of HS-mPEG was needed to make brush conformation based on the calculation (see the Supporting Information). We used 10 mg, 2 mg, 1 mg, 1 μg, and 0.5 μg of HS-mPEG for ligand exchange of the GNRs. The PDA coating on the surface of GNR was unstable when we used 1 and 0.5 μg of HS-mPEG, while PDA coating became uniform and stable when we used 10, 2, and 1 mg of HS-mPEG (Figure 2B,C), indicating that the brush conformation is an ideal condition for the PDA coating. ζ potential data showed that all PEGylated GNRs had a less positive charged surface compared to the CTAB-stabilized GNRs (Figure 2D). Furthermore, PEGylated GNRs with the brush conformation showed improved colloidal stability due to the steric effect and slightly negatively charged PEG (Figure S1).

The formation of PDA coating is easily induced by polymerization of dopamine under alkaline conditions. Under basic conditions (pH > 7.5), dopamine is first oxidized to the reactive dopamine quinones[47] that undergo successive oxidation, intramolecular cyclization, oligomerization, and self-assembly to form PDA.[42,48,49] Together with the universal adhesive properties of PDA, we uniformly coated PDA on the surface of the PEGylated GNRs probably due to metal chelation and hydrogen bonding.[50] TEM and SEM clearly showed monodisperse GNR@PDA nanohybrids in aqueous solution (Figures 2E–G and S2) in bicine buffer (pH 8.5). The PDA thicknesses were easily tunable from 15 to 150 nm by adjusting the amount of dopamine feed (4 mg/mL) used for the reaction (Table 1). GNRs with PDA thicknesses of 15, 25, 50, and 70 nm (referred to as GNR@PDA15, GNR@PDA25, GNR@PDA50, and GNR@PDA70, respectively) were formed by controlling the amount of dopamine used at a fixed GNR concentration (Figure 2C,E–G),

but the GNRs aggregated when we added excess dopamine (2.4 mg of dopamine was added to 40 μg of GNRs).

The color of the solution changed from brown to black and became darker as more dopamine was added (Figure 2H). GNR@PDA showed broadband optical extinction from the UV and visible to NIR spectral range, and the light extinction was proportional to the PDA thickness versus GNRs that featured a longitudinal LSPR at 1090 nm, and the absorption peaks red-shifted to 1246, 1284, 1286, and 1284 nm for GNR@PDA15, GNR@PDA25, GNR@PDA50, and GNR@PDA70, respectively. Moreover, longitudinal peaks of GNR@PDA in the NIR-II range were no longer distinguished when the PDA thickness became 150 nm (Figure S3). EDX mapping indicated that GNR@PDA nanohybrids were composed of Au, C, N, and O confirming the core–shell nanostructure of the GNR–melanin hybrids (Figure 2I). ζ potential data revealed that the PEGylated GNRs became more negatively charged after PDA coating due to the negative charge of the PDA (Figure 2J). DLS data showed that GNR@PDA25, GNR@PDA50, and GNR@PDA70 had relatively narrow size distributions [polydispersity index (PDI) < 0.1], and the size of the GNR@PDA nanohybrids increased with thicker PDA coating (Figure 2K).

PA Performance of GNR@PDAs.

The PA signal and excitation energy are influenced by nanoparticle concentration.[51] Thus, we used ICP-MS to measure GNR concentration according to the number of Au ions in each sample (Figure S4). UV–vis–NIR absorption spectra data showed that the GNR exhibited two absorption peaks at 512 and 1090 nm, which correspond to the transverse and longitudinal LSPR, respectively (Figure 2L). The longitudinal peak of the GNR was significantly red-shifted when PDA was coated due to the increased refractive index (n) of the surrounding medium ($n_{\mathrm{PDA}} \approx 1.7$) compared to the GNRs that were surrounded by water ($n_{\mathrm{H_2O}} \approx 1.3$).[52] More importantly, the optical extinction of GNR@PDAs was higher than GNRs due to the absorbance of melanin and the increased size of hybrid nanoparticles. The increase in absorption intensity is important because PA efficiency is a function of the optical and thermoelastic properties of the nanoparticles. The mechanism of PA signal generation has been understood by the thermoelastic expansion model according to eq 1.[1,13]

$$\rho_{\mathrm{o}} = \left(\frac{\beta c^2}{C_p}\right)\mu_\alpha F \tag{1}$$

where ρ_{o}, β, c^2, C_p, μ_a, and F are pressure gradient, thermoelastic expansion coefficient, speed of sound in the medium, specific heat capacity, absorption coefficient, and laser fluence, respectively. According to this mechanism, photons absorbed by nanoparticles are converted to heat with an increase in temperature, leading to thermoelastic expansion. This expansion generates transient acoustic waves that can be measured using an ultrasound transducer.[51]

To understand the PA performance of GNR@PDA systems, we first used an NIR-I laser where PDA largely absorbs light (GNRs have small absorption in the NIR-I window). Figure 3A,B shows a PA image and its corresponding quantitative PA intensity of GNRs and GNR@PDAs when irradiated at 680 nm. PA signals of GNR@PDA25, GNR@PDA50, and

GNR@PDA70 were at least twofold higher than that of pristine GNRs under 680 nm laser irradiation. In addition, GNR@PDAs with thicker PDA coating showed a higher PA signal amplitude: GNR@PDA50 showed a fourfold higher PA signal than GNR@PDA15 at the same gold mass concentration (0.04 μg/mL).

This increase in PA signal can be understood *via* three parameters: optical absorption, absorption cross-sectional area, and photothermal conversion efficiency. First, melanin-like PDA coating on GNRs showed at least twofold higher optical absorption (Figure 2L), and absorption is proportional to the PA signal amplitude. Both the GNR core and its PDA coating of GNR@PDA absorbed photons. Thus, the GNR@PDAs absorbed twofold more photons than pristine GNRs alone. Second, the absorption cross-sectional area of GNR@PDA, as measured by electron microscopy, was larger than the GNRs. More specifically, the absorption cross-sectional area of GNR@PDA15 was fourfold larger than that of GNR. The cross-sectional area became larger as the PDA coating became thicker (Figure S5).

Finally, thermal confinement from the PDA shell contributes to the PA signal.[53] Thermal energy that increased in the nanoparticles diffuses to the surrounding medium during the photon absorption. Thus, thermal expansion of the nanoparticles is influenced by their surrounding environment. The heat capacity of water $\left(C_{p,\mathrm{H_2O}} \approx 4.2\right)$ is 2.5-fold higher than that of PDA ($C_{p,\mathrm{PDA}} \approx 1.6$), indicating that the GNR surrounded by water is more easily cooling down versus the GNR surrounded by PDA.[54] Therefore, GNR@PDA can have higher thermoelastic expansion than GNR due to its lower heat capacity of the surrounding condition (see eq 1). In addition, the thermal conductivity of water $\left(k_{\mathrm{H_2O}} \approx 0.59\right)$ is fourfold larger than PDA ($k_{\mathrm{PDA}} \approx 0.13$), meaning that heat accumulation easily occurs in GNR@PDA *via* reduced thermal conductance.[54]

We then evaluated the PA signal generation of GNR@PDA in the NIR-II window where GNRs have a large optical absorption. Figure 3C,D shows PA images and the corresponding quantitative PA intensity when irradiated at 1064 nm. GNR@PDAs showed similar results to in 680 nm: GNR@PDA25, GNR@PDA50, and GNR@PDA70 had a higher PA signal than pristine GNRs, and the PA signal amplitude increased as the PDA coating became thicker. Interestingly, GNR@PDA15 showed a weaker PA signal than GNR. GNR@PDA15 had a twofold lower absorption coefficient at 1064 nm versus GNRs because of the red-shifted absorption peak (Figure 2L). This result indicates that the optical absorption of the nanoparticle largely affects PA signal generation. In addition to the optical absorption, the laser fluence (F) also plays an important role in generating the PA signal (see eq 1). The laser fluence at 680 nm was 3 mJ higher than at 1064 nm, and the GNR and GNR@PDA nanohybrids showed a higher PA signal at 680 nm than at 1064 nm (Figure 3B,D). Finally, the optical extinction of GNR linearly increased with elevated concentration according to the Beer–Lambert law[55] (Figure S6), thus leading to a linear increase in PA signal of GNR and GNR@PDA50 at 1064 nm irradiation (Figure 3E,F).

Thermal and Structural Stability of GNR@PDAs.

Under the laser illumination, free electrons undergo a collective dipolar oscillation, generating high local heat energy that leads to the migration of atoms at {110} facets[26,56] (Figure S8). The atomic rearrangement transforms the anisotropic structure of GNRs into a spherical shape that can minimize surface energy (Figure S8). The shape transition of GNRs can also be explained by the absorbance decrease according to eq 2.[57]

$$\left[\left(A_{\lambda,0} - A_{\lambda,1}\right)/\sigma b\right] = \rho\sigma^{(n)}I^{(n)} \tag{2}$$

where $A_{\lambda,0}$ is the sample absorbance at a given wavelength (λ) before the laser illumination, $A_{\lambda,1}$ is the sample absorbance at a given wavelength (λ) after the laser illumination, σ is the absorption cross section of the nanoparticles, b is the path length, ρ is the density of the nanoparticles, and n is the number of photons absorbed. I is laser fluence. Equation 2 can be rearranged to (see the Supporting Information)

$$\ln\left[\left(A_{\lambda,0} - A_{\lambda,1}\right)/A_{\lambda,0}\right] = n\ln(I) + \text{ constant} \tag{3}$$

where $(A_{\lambda,0} - A_{\lambda,1})/A_{\lambda,0}$ represents the percentage of absorbance changes during the laser illumination. Hence, the shape transition of GNRs was confirmed by a decrease in optical extinction during the laser illumination (Figure 4A). The longitudinal peak of GNRs exhibited an 84% decrease in intensity and was blue-shifted after 5 min of the illumination, which corresponds to the TEM observations where most GNRs became spherical (Figure 4B). In contrast, GNRs covered by a PDA shell retained their rodlike shape and optical extinction. Specifically, GNRs with a PDA thickness of 50 nm (referred to as GNR@PDA50) maintained their rod shapes, and the longitudinal peak of GNR@PDA50 showed a 11% decrease in intensity after 5 min of illumination (Figure 4C,D). In addition, the longitudinal peaks of GNR@PDAs weakened less with increasing PDA coating thickness. Longitudinal peaks of GNR@PDA15, GNR@PDA25, and GNR@PDA70 decreased by 47, 33, and 9%, respectively, and maintained their rodlike shape (Figures S9 and S10). PDA coating did not melt even after 15 min of laser illumination (Figure S11).

The PDA coating prohibits the photon-induced shape transition process and improves the thermal stability of GNRs. GNRs with a thicker PDA coating showed less of a drop in optical absorption at 680 and 1064 nm (Figure 4E); GNR@PDA15, GNR@PDA25, GNR@PDA50, and GNR@PDA70 showed 48, 42, 15, and 10% drop, respectively, in absorbance at a wavelength of 1064 nm after 5 min of laser illumination. We also monitored the PA intensity of GNR and GNR@PDAs during laser illumination. The PA signal amplitude of GNR decreased by 73% after 5 min, while GNR@PDA15, GNR@PDA25, GNR@PDA50, and GNR@PDA70 decreased by 44, 35, 40, and 25%, respectively (Figure 4F).

We hypothesize that PDA coating can stabilize the GNRs from the shape transition for two main reasons. First, the stiffness and chemical properties of the surrounding medium affect the shape transition.[26,58] Gold atoms on the surface of GNR@PDAs are tightly pinned because of the aromatic PDA shell that is highly cross-linked and the π-stacked dense structure.[59,60] Thus, PDA coating makes a physical barrier for atomic rearrangement in the

GNRs, requiring more energy, and retards the surface atom diffusivity. In addition, Ostwald ripening also influences shape transition. PDA coating increases activation energy for dissolution and redeposition processes in the Ostwald ripening, thus preventing shape transition of GNRs.[61] Poly(styrenesulfonate)-coated GNRs showed a similar result that shape transition of GNR@PSS was prevented due to the retardation of the Ostwald ripening.[61] Second, shape transition of GNR is due to the amount of fluence incident on the GNRs (eq 3). The PDA coating absorbs photons and reduces the fluence on the GNRs. Thus, GNRs covered by the PDA shell are damaged less than pristine GNRs.

PA Performance of Rod-Shaped PDA Capsules.

Next, we studied the PA performance of PDA shells alone to better understand their contribution to the hybrid system. The GNR core was removed with a Cu^{2+}-mediated method where Cu ions formed AuCu alloys in the DMF solvent, leading to a decrease in Au stability.[62] After centrifugation to remove surfactants, we enabled to synthesize rod-shaped PDA hollow capsules with 15, 25, 50, and 70 nm shell thicknesses (referred to as $PDA_{capsule}15$, $PDA_{capsule}25$, $PDA_{capsule}50$, and $PDA_{capsule}70$, respectively). TEM data clearly showed that PDA capsules had a rodlike cavity inside, indicating that the GNR core was removed by the Cu ions (Figure 5A–D).

UV–vis–NIR absorption spectral data revealed that rod-shaped PDA capsules had a broadband optical absorption but no longitudinal absorption peak in the NIR II window (Figure 5I). The absorption intensity of the PDA capsule again increased with a thicker shell thickness. $PDA_{capsule}70$ showed a fivefold higher intensity than $PDA_{capsule}25$. We then studied PA performance of PDA capsules from 680 to 1064 nm illuminations (Figure 5J). PDA capsules exhibited a threefold higher PA signal at 680 nm than at 1064 nm due to the 4.4-fold higher optical absorption and stronger laser fluence at 680 nm. In addition, a thicker PDA capsule had a higher PA intensity than a thinner PDA capsule. For instance, $PDA_{capsule}70$ had twofold higher PA intensity than $PDA_{capsule}25$ (Figure 5J), and $PDA_{capsule}50$ showed 40% of PA intensity of its original structure (*e.g.*, GNR@PDA50). This suggests that PDA alone can produce the PA signal but that there is a synergetic effect in PA signal generation when the capsule is combined with GNR. Moreover, this PDA coating strategy can be applied to diverse nanoparticles *via* the adhesive property of PDA for improving PA imaging (Figure S13). By virtue of this binding ability, PDA can load a variety of materials (*e.g.*, 6.4% for Gd(III) by Lemaster *et al.*[49] and 37.4% for doxorubicin by Li *et al.*[63]) because of the catechol groups in PDA.[36] Thus, PDA coating can deliver the photosensitizer for photodynamic therapy.[22] Additionally, the GNR@PDA probe showed 2% higher photothermal conversion efficiency than GNR, indicating that PDA coating can serve as an excellent photothermal transducer for photothermal therapy (Figure S14).

In Vivo Stability Test of GNR@PDA.

Finally, we conducted *in vivo* experiments of GNR@PDA to investigate PA signal stability in biological samples. We first implanted GNR and GNR@PDA in 50% Matrigel (150 μL). The same mass of gold was used for both GNR and GNR@PDA50 (0.2 μg/mL). The material was subcutaneously injected into the mice ($n = 3$) and imaged 10 min after the injection. We can clearly see the anatomical images from the B-mode (ultrasound) and

confirm that the PA signal was from our GNR@PDA probes (Figure 6A,B). Surprisingly, GNR@PDA50 maintained 87% of its original PA signal even after 10 min of laser illumination, while there was no PA signal of the GNR likely due to the shape deformation and background scattering (Figure 6C). Furthermore, PA intensity of GNR@PDA was 10-fold higher than the bare GNR ($p < 0.0001$), indicating that PDA coating can improve PA performance of GNR in the NIR-II window (Figure 6D). These results are consistent with our *in vitro* experiments (Figures 3D and 4F).

The colloidal stability of GNR@PDA50 was further studied in different media (*e.g.*, 10 mM HCl, 10 mM NaOH, 10 mM NaCl, and DMEM with 20, 10, or 5% of mouse serum). DLS data showed that GNR@PDA50 had a high colloidal stability in NaCl, 20% mouse serum, pH 2 and 12 (PDI < 0.1). Negligible aggregation or disassembly of PDA coating was found under these conditions (Figure 6E). These results indicate that PDA coating is highly robust and stable under biological or extreme conditions, which might be due to abundant catechol and amino groups in PDA and its covalently cross-linked structure.[36] Therefore, our PDA coating strategy not only leads to outstanding PA performance over the original GNR probe but also gives these nanoparticles excellent colloidal stability under diverse biological conditions.

CONCLUSIONS

A stable PA signal is essential to achieve high-quality and reliable imaging in biomedical applications. In this study, we synthesized GNR–melanin hybrids (*i.e.*, GNR@PDA) with a tunable PDA protective coating to overcome the poor thermal stability of GNR. By virtue of the robust PDA structure, GNR@PDAs showed enhanced structural and thermal stability than pristine GNRs. Specifically, GNR@PDAs showed an improved structural integrity of the built-in GNR core and a twofold higher signal even after 5 min of laser illumination. PDA coating can provide a synergetic effect in improving optical absorption, thermal confinement, and absorption cross-sectional area, leading to a threefold stronger PA signal than GNR. Surprisingly, GNR@PDA still generated 87% of its original PA signal *in vivo* even after 10 min of laser illumination unlike bare GNRs that decreased by 75%. Furthermore, our nanoprobe showed a high colloidal stability under biological conditions. These findings highlight the potential use of PDA coating in developing photomediated contrast agents in a broad spectral range including the NIR-II window and expand on understanding the PA mechanism occurring in the nanoparticles. Moreover, this PDA coating strategy not only gives opportunities for other types of photomeditated biomedicines but also holds high potential as nanocarriers in living subjects.

Supplementary Material

Refer to Web version on PubMed Central for supplementary material.

ACKNOWLEDGMENTS

The authors acknowledge the National Science Foundation under awards 1845683 and 1937674. We also acknowledge National Institutes of Health under awards DP2 HL 137187, R21 DE029917, and R21 AI157957. The authors also acknowledge infrastructure support under awards S10 OD021821 and S10 OD023555. M.N.C. acknowledges fellowship funding under NIH award T32 CA153915. This material is based upon work supported by

the NSF Graduate Research Fellowship Program under grant no. DGE-1650112. Transmission electron micrographs were taken in the Cellular and Molecular Medicine Electron Microscopy Core Facility, which is supported in part by National Institutes of Health award number S10 OD023527.

REFERENCES

(1). Xu M; Wang LV Photoacoustic Imaging in Biomedicine. Rev. Sci. Instrum 2006, 77, 041101.

(2). Mallidi S; Luke GP; Emelianov S Photoacoustic Imaging in Cancer Detection, Diagnosis, and Treatment Guidance. Trends Biotechnol. 2011, 29, 213–221. [PubMed: 21324541]

(3). Cheng MHY; Mo Y; Zheng G Nano Versus Molecular: Optical Imaging Approaches to Detect and Monitor Tumor Hypoxia. Adv. Healthcare Mater 2020, 10, 2001549.

(4). Huang J; Pu K Activatable Molecular Probes for Second Near-Infrared Fluorescence, Chemiluminescence, and Photoacoustic Imaging. Angew. Chem., Int. Ed 2020, 132, 11813–11827.

(5). Moore C; Chen F; Wang J; Jokerst JV Listening for the Therapeutic Window: Advances in Drug Delivery utilizing Photoacoustic Imaging. Adv. Drug Delivery Rev. 2019, 144, 78–89.

(6). Mishra K; Fuenzalida-Werner JP; Ntziachristos V; Stiel AC Photocontrollable Proteins for Optoacoustic Imaging. Anal. Chem 2019, 91, 5470–5477. [PubMed: 30933491]

(7). Jeevarathinam AS; Lemaster JE; Chen F; Zhao E; Jokerst JV Photoacoustic Imaging Quantifies Drug Release from Nanocarriers via Redox Chemistry of Dye-Labeled Cargo. Angew. Chem., Int. Ed 2020, 59, 4678–4683.

(8). Chen F; Zhao ER; Hableel G; Hu T; Kim T; Li J; Gonzalez-Pech NI; Cheng DJ; Lemaster JE; Xie Y; Grassian VH; Sen GL; Jokerst JV Increasing the Efficacy of Stem Cell Therapy via Triple-Function Inorganic Nanoparticles. ACS Nano 2019, 13, 6605–6617. [PubMed: 31188564]

(9). Pu K; Shuhendler AJ; Jokerst JV; Mei J; Gambhir SS; Bao Z; Rao J Semiconducting Polymer Nanoparticles as Photoacoustic Molecular Imaging Probes in Living Mice. Nat. Nanotechnol 2014, 9, 233–239. [PubMed: 24463363]

(10). Weber J; Beard PC; Bohndiek SE Contrast Agents for Molecular Photoacoustic Imaging. Nat. Methods 2016, 13, 639–650. [PubMed: 27467727]

(11). Dreaden EC; Alkilany AM; Huang X; Murphy CJ; El-Sayed MA The Golden Age: Gold Nanoparticles for Biomedicine. Chem. Soc. Rev 2012, 41, 2740–2779. [PubMed: 22109657]

(12). Liu Y; He J; Yang K; Yi C; Liu Y; Nie L; Khashab NM; Chen X; Nie Z Folding up of Gold Nanoparticle Strings into Plasmonic Vesicles for Enhanced Photoacoustic Imaging. Angew. Chem., Int. Ed 2015, 54, 15809–15812.

(13). Mantri Y; Jokerst JV Engineering Plasmonic Nanoparticles for Enhanced Photoacoustic Imaging. ACS Nano 2020, 14, 9408–9422. [PubMed: 32806027]

(14). Jain PK Gold Nanoparticles for Physics, Chemistry, and Biology. edited by Catherine Louis and Olivier Pluchery. Angew. Chem., Int. Ed 2014, 53, 1197.

(15). Chen Y-S; Zhao Y; Yoon SJ; Gambhir SS; Emelianov S Miniature Gold Nanorods for Photoacoustic Molecular Imaging in the Second Near-Infrared Optical Window. Nat. Nanotechnol 2019, 14, 465–472. [PubMed: 30833692]

(16). SoRelle ED; Liba O; Hussain Z; Gambhir M; de la Zerda A Biofunctionalization of Large Gold Nanorods realizes Ultrahigh-Sensitivity Optical Imaging Agents. Langmuir 2015, 31, 12339–12347. [PubMed: 26477361]

(17). Busbee BD; Obare SO; Murphy CJ An Improved Synthesis of High-Aspect-Ratio Gold Nanorods. Adv. Mater 2003, 15, 414–416.

(18). Mantri Y; Davidi B; Lemaster JE; Hariri A; Jokerst JV Iodide-Doped Precious Metal Nanoparticles: Measuring Oxidative Stress In Vivo via Photoacoustic Imaging. Nanoscale 2020, 12, 10511–10520. [PubMed: 32396928]

(19). Jiang Y; Upputuri PK; Xie C; Zeng Z; Sharma A; Zhen X; Li J; Huang J; Pramanik M; Pu K Metabolizable Semiconducting Polymer Nanoparticles for Second Near-Infrared Photoacoustic Imaging. Adv. Mater 2019, 31, 1808166.

(20). Ma L; Huang S; He S; Wang Z; Cheng Z Polydopamine-coated Downconversion Nanoparticle as an Efficient Dual-Modal Near-Infrared-II Fluorescence and Photoacoustic Contrast Agent for

Non-Invasive Visualization of Gastrointestinal Tract In Vivo. Biosens. Bioelectron 2020, 151, 112000. [PubMed: 31999595]

(21). Liu Y; Liu H; Yan H; Liu Y; Zhang J; Shan W; Lai P; Li H; Ren L; Li Z; Nie L Aggregation-Induced Absorption Enhancement for Deep Near-Infrared II Photoacoustic Imaging of Brain Gliomas In Vivo. Adv. Sci 2019, 6, 1801615.

(22). Chen R; Huang S; Lin T; Ma H; Shan W; Duan F; Lv J; Zhang J; Ren L; Nie L Photoacoustic Molecular Imaging-Escorted Adipose Photodynamic–Browning Synergy for Fighting Obesity with Virus-like Complexes. Nat. Nanotechnol 2021, 1–11.

(23). Antaris AL; Chen H; Cheng K; Sun Y; Hong G; Qu C; Diao S; Deng Z; Hu X; Zhang B; Zhang X; Yaghi OK; Alamparambil ZR; Hong X; Cheng Z; Dai H A Small-Molecule Dye for NIR-II Imaging. Nat. Mater 2016, 15, 235–242. [PubMed: 26595119]

(24). Jiang Y; Zhao X; Huang J; Li J; Upputuri PK; Sun H; Han X; Pramanik M; Miao Y; Duan H Transformable Hybrid Semiconducting Polymer Nanozyme for Second Near-Infrared Photothermal Ferrotherapy. Nat. Commun 2020, 11, 1857. [PubMed: 32312987]

(25). Ding X; Liow CH; Zhang M; Huang R; Li C; Shen H; Liu M; Zou Y; Gao N; Zhang Z; Li Y; Wang Q; Li S; Jiang J Surface Plasmon Resonance Enhanced Light Absorption and Photothermal Therapy in the Second Near-Infrared Window. J. Am. Chem. Soc 2014, 136, 15684–15693. [PubMed: 25340966]

(26). Chang S-S; Shih C-W; Chen C-D; Lai W-C; Wang CRC. The Shape Transition of Gold Nanorods. Langmuir 1999, 15, 701–709.

(27). Link S; Wang ZL; El-Sayed MA How does a Gold Nanorod Melt? J. Phys. Chem. B 2000, 104, 7867–7870.

(28). Link S; Burda C; Nikoobakht B; El-Sayed MA Laser-Induced Shape Changes of Colloidal Gold Nanorods Using Femtosecond and Nanosecond Laser Pulses. J. Phys. Chem. B 2000, 104, 6152–6163.

(29). Albrecht W; Deng T-S; Goris B; van Huis MA; Bals S; van Blaaderen A Single Particle Deformation and Analysis of Silica-Coated Gold Nanorods Before and After Femtosecond Laser Pulse Excitation. Nano Lett. 2016, 16, 1818–1825. [PubMed: 26871607]

(30). Chen L-C; Wei C-W; Souris JS; Cheng S-H; Chen C-T; Yang C-S; Li P-C; Lo L-W Enhanced Photoacoustic Stability of Gold Nanorods by Silica Matrix Confinement. J. Biomed. Opt 2010, 15, 016010. [PubMed: 20210456]

(31). Bae C; Lee J; Yao L; Park S; Lee Y; Lee J; Chen Q; Kim J Mechanistic Insight into Gold Nanorod Transformation in Nanoscale Confinement of ZIF-8. Nano Res. 2020, 14, 66–73.

(32). Qi C; Fu L-H; Xu H; Wang T-F; Lin J; Huang P Melanin/Polydopamine-based Nanomaterials for Biomedical Applications. Sci. China: Chem 2019, 62, 162–188.

(33). Lee H; Dellatore SM; Miller WM; Messersmith PB Mussel-Inspired Surface Chemistry for Multifunctional Coatings. Science 2007, 318, 426–430. [PubMed: 17947576]

(34). Battistella C; McCallum NC; Vanthournout B; Forman CJ; Ni QZ; La Clair JJ; Burkart MD; Shawkey MD; Gianneschi NC Bioinspired Chemoenzymatic Route to Artificial Melanin for Hair Pigmentation. Chem. Mater 2020, 32, 9201–9210.

(35). Schanze KS; Lee H; Messersmith PB Ten Years of Polydopamine: Current Status and Future Directions. ACS Appl. Mater. Interfaces 2018, 10, 7521–7522. [PubMed: 29510631]

(36). Wu D; Zhou J; Creyer MN; Yim W; Chen Z; Messersmith PB; Jokerst JV Phenolic-Enabled Nanotechnology: Versatile Particle Engineering for Biomedicine. Chem. Soc. Rev 2021, DOI: 10.1039/D0CS00908C.

(37). Zhou J; Lin Z; Ju Y; Rahim MA; Richardson JJ; Caruso F Polyphenol-Mediated Assembly for Particle Engineering. Acc. Chem. Res 2020, 53, 1269–1278. [PubMed: 32567830]

(38). Zhou J; Jiang Y; Hou S; Upputuri PK; Wu D; Li J; Wang P; Zhen X; Pramanik M; Pu K; Duan H Compact Plasmonic Blackbody for Cancer Theranosis in the Near-Infrared II Window. ACS Nano 2018, 12, 2643–2651. [PubMed: 29438610]

(39). Hong S; Kim KY; Wook HJ; Park SY; Lee KD; Lee DY; Lee H Attenuation of the In Vivo Toxicity of Biomaterials by Polydopamine Surface Modification. Nanomedicine 2011, 6, 793–801. [PubMed: 21793672]

(40). Ryu J; Ku SH; Lee H; Park CB Mussel-Inspired Polydopamine Coating as a Universal Route to Hydroxyapatite Crystallization. Adv. Funct. Mater 2010, 20, 2132–2139.

(41). Huang W; Chen R; Peng Y; Duan F; Huang Y; Guo W; Chen X; Nie L In vivo Quantitative Photoacoustic Diagnosis of Gastric and Intestinal Dysfunctions with a Broad pH-Responsive Sensor. ACS Nano 2019, 13, 9561–9570. [PubMed: 31361949]

(42). Zhou J; Xiong Q; Ma J; Ren J; Messersmith PB; Chen P; Duan H Polydopamine-Enabled Approach toward Tailored Plasmonic Nanogapped Nanoparticles: from Nanogap Engineering to Multifunctionality. ACS Nano 2016, 10, 11066–11075. [PubMed: 28024348]

(43). Kim T; Zhang Q; Li J; Zhang L; Jokerst JV A Gold/Silver Hybrid Nanoparticle for Treatment and Photoacoustic Imaging of Bacterial Infection. ACS Nano 2018, 12, 5615–5625. [PubMed: 29746090]

(44). Schneider CA; Rasband WS; Eliceiri KW NIH Image to ImageJ: 25 years of Image Analysis. Nat. Methods 2012, 9, 671–675. [PubMed: 22930834]

(45). de Gennes PG Conformations of Polymers Attached to an Interface. Macromolecules 1980, 13, 1069–1075.

(46). Jokerst JV; Lobovkina T; Zare RN; Gambhir SS Nanoparticle PEGylation for Imaging and Therapy. Nanomedicine 2011, 6, 715–728. [PubMed: 21718180]

(47). Lemaster JE; Jeevarathinam AS; Kumar A; Chandrasekar B; Chen F; Jokerst JV Synthesis of Ultrasmall Synthetic Melanin Nanoparticles by UV Irradiation in Acidic and Neutral Conditions. ACS Appl. Bio Mater 2019, 2, 4667–4674.

(48). Zhang L; Su H; Cai J; Cheng D; Ma Y; Zhang J; Zhou C; Liu S; Shi H; Zhang Y; Zhang C A Multifunctional Platform for Tumor Angiogenesis-Targeted Chemo-Thermal Therapy using Polydopamine-coated Gold Nanorods. ACS Nano 2016, 10, 10404–10417. [PubMed: 27934087]

(49). Lemaster JE; Wang Z; Hariri A; Chen F; Hu Z; Huang Y; Barback CV; Cochran R; Gianneschi NC; Jokerst JV Gadolinium Doping enhances the Photoacoustic Signal of Synthetic Melanin Nanoparticles: a Dual Modality Contrast Agent for Stem Cell Imaging. Chem. Mater 2018, 31, 251–259. [PubMed: 33859455]

(50). Zmerli I; Michel J-P; Makky A Bioinspired Polydopamine Nanoparticles: Synthesis, Nanomechanical Properties, and Efficient PEGylation Strategy. J. Mater. Chem. B 2020, 8, 4489–4504. [PubMed: 32365146]

(51). Wang S; Fu L; Xin J; Wang S; Yao C; Zhang Z; Wang J Photoacoustic Response Induced by Nanoparticle-Mediated Photothermal Bubbles beyond the Thermal Expansion for Potential Theranostics. J. Biomed. Opt 2018, 23, 125002.

(52). Zhang C; Wu B-H; Du Y; Ma M-Q; Xu Z-K Mussel-Inspired Polydopamine Coatings for Large-Scale and Angle-Independent Structural Colors. J. Mater. Chem. C 2017, 5, 3898–3902.

(53). Shi Y; Qin H; Yang S; Xing D Thermally Confined Shell Coating amplifies the Photoacoustic Conversion Efficiency of Nanoprobes. Nano Res. 2016, 9, 3644–3655.

(54). Repenko T; Rix A; Nedilko A; Rose J; Hermann A; Vinokur R; Moli S; Cao-Milàn R; Mayer M; von Plessen G; Fery A; De Laporte L; Lederle W; Chigrin DN; Kuehne AJC Strong Photoacoustic Signal Enhancement by Coating Gold Nanoparticles with Melanin for Biomedical Imaging. Adv. Funct. Mater 2018, 28, 1705607.

(55). Swinehart DF The Beer-Lambert Law. J. Chem. Educ 1962, 39, 333–335.

(56). Brorson SD; Fujimoto JG; Ippen EP Femtosecond Electronic Heat-Transport Dynamics in Thin Gold Films. Phys. Rev. Lett 1987, 59, 1962. [PubMed: 10035379]

(57). Gandhi SR; Bernstein RB Influence of the Focal Length of the Laser Beam Focusing le ns on MPI yield. Chem. Phys 1986, 105, 423–434.

(58). Centi S; Cavigli L; Borri C; Milanesi A; Banchelli M; Chioccioli S; Khlebtsov BN; Khlebtsov NG; Matteini P; Bogani P; Ratto F; Pini R Small Thiols stabilize the Shape of Gold Nanorods. J. Phys. Chem. C 2020, 124, 11132–11140.

(59). Postma A; Yan Y; Wang Y; Zelikin AN; Tjipto E; Caruso F Self-Polymerization of Dopamine as a Versatile and Robust Technique to Prepare Polymer Capsules. Chem. Mater 2009, 21, 3042–3044.

(60). Zhou J; Lin Z; Penna M; Pan S; Ju Y; Li S; Han Y; Chen J; Lin G; Richardson JJ Particle Engineering Enabled by Polyphenol-Mediated Supramolecular Networks. Nat. Commun. 2020, 11, 4804. [PubMed: 32968077]

(61). Zou R; Zhang Q; Zhao Q; Peng F; Wang H; Yu H; Yang J Thermal Stability of Gold Nanorods in an Aqueous Solution. Colloids Surf., A 2010, 372, 177–181.

(62). Huang Z; Raciti D; Yu S; Zhang L; Deng L; He J; Liu Y; Khashab NM; Wang C; Gong J; Nie Z Synthesis of Platinum Nanotubes and Nanorings via Simultaneous Metal Alloying and Etching. J. Am. Chem. Soc 2016, 138, 6332–6335. [PubMed: 27090384]

(63). Li W; Hu J; Wang J; Tang W; Yang W; Liu Y; Li R; Liu H Polydopamine-Mediated Polypyrrole/Doxorubicin Nanocomplex for Chemotherapy-Enhanced Photothermal Therapy in Both NIR-I and NIR-II Biowindows against Tumor Cells. J. Appl. Polym. Sci 2020, 137, 49239.

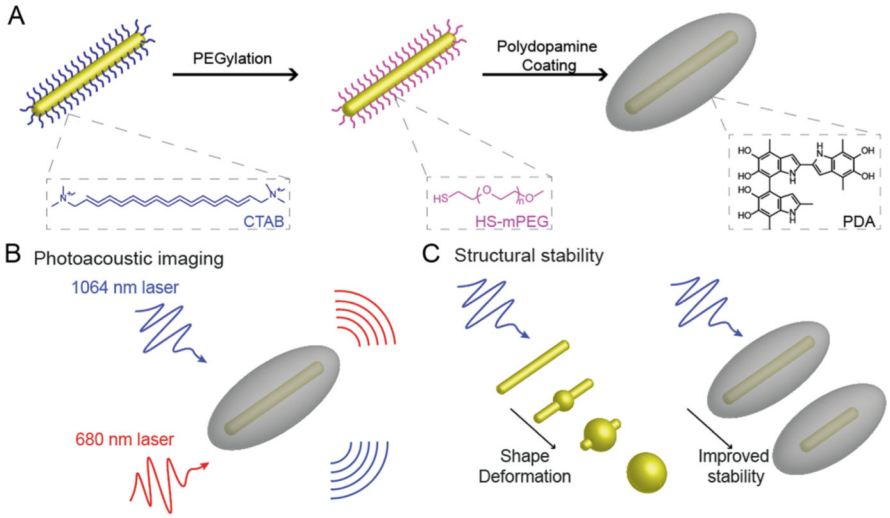

Figure 1.

(A) Schematic of the synthesis of GNR@PDA. (B) Comparative PA signals generated by GNR@PDAs at NIR-I (*e.g.*, 680 nm) and NIR-II (*e.g.*, 1064 nm) irradiations. (C) Morphological deformation of GNR when exposed to the high-fluence pulsed laser, while GNR@PDAs show the enhanced structural and thermal stability.

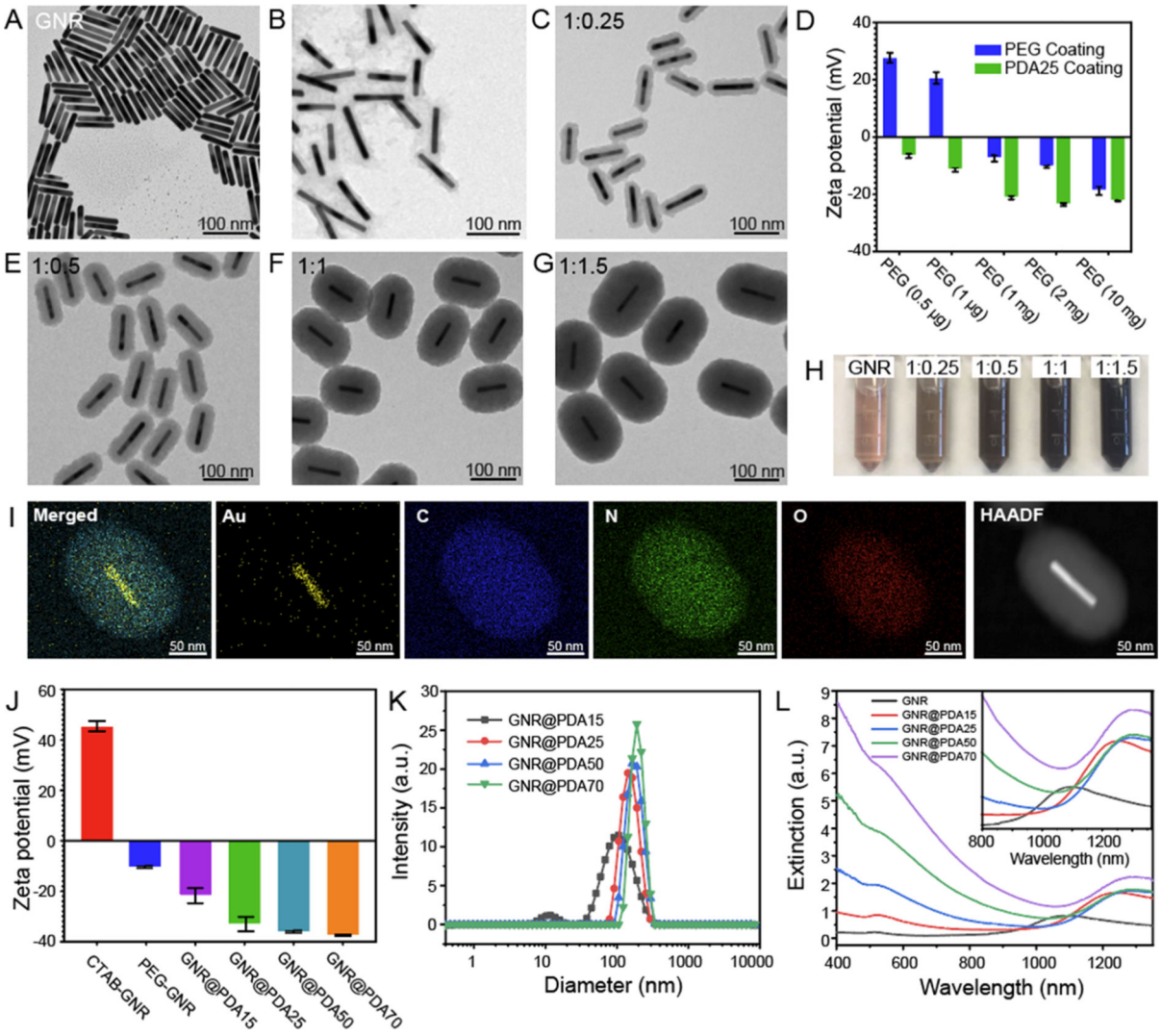

Figure 2.

Controllable size of GNR@PDA. (A) TEM images of GNRs. (B,C) TEM images of PDA-coated GNRs where PEG chains had (B) mushroom and (C) brush conformations. (D) ζ potential of PEGylated GNRs before and after PDA coating (PDA thickness = 25 nm). We used different amounts of HS-mPEG (10 mg, 2 mg, 1 mg, 1 μg, and 0.5 μg) for ligand exchange of the GNRs to make either mushroom or brush conformations of PEG chains. (C,E–F) TEM images with different PDA thicknesses: (C) 15, (E) 25, (F) 50, and (G) 70 nm. The mass concentration of GNR was fixed at 0.2 μg/mL, and 1:0.25, 1:0.5, 1:1, and 1:1.5 indicate the mass ratio of GNR to dopamine concentrations. (H) Color of GNR and GNR@PDA solutions. (I) EDX and high-angle annular dark-field images of GNR@PDA. The EDX result shows the core–shell nanostructure of GNR@PDA. GNR@PDA includes gold (Au), carbon (C), nitrogen (N), and oxygen (O). (J) ζ potential of GNR and GNR@PDAs. (K) DLS measurements of GNR@PDA15, GNR@PDA25, GNR@PDA50, and GNR@PDA70. (L) UV–vis–NIR absorption spectra of GNR and GNR@PDAs. Gray, red, blue, green, and purple lines represent GNR, GNR@PDA15, GNR@PDA25, GNR@PDA50, and GNR@PDA70, respectively. The inset image is the magnified

absorption spectra from 800 to 1350 nm. The error bar represents standard deviation of five measurements.

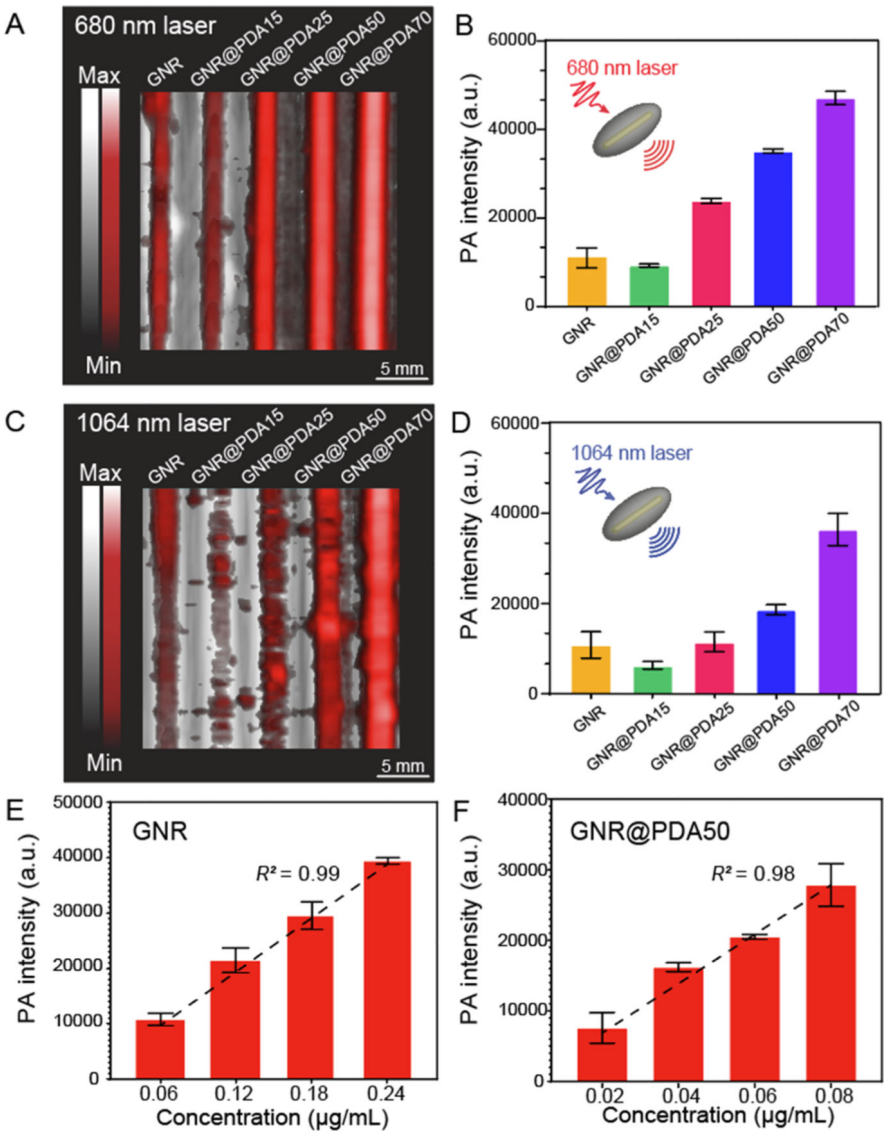

Figure 3.

PA performance of GNR and GNR@PDA. (A,B) PA image and its corresponding PA intensity when illuminated by a 680 nm laser. (C,D) PA image and its corresponding PA intensity when illuminated by a 1064 nm laser. GNR@PDAs showed a higher PA signal amplitude than pristine GNRs. (E) PA intensity of GNR and (F) PA intensity of GNR@PDA50 with the elevated concentration when illuminated by a 1064 nm laser. Figure S7 shows the PA intensity of GNR@PDA50 irradiated by a 680 nm laser. The error bars represent the standard deviation of five regions of interest.

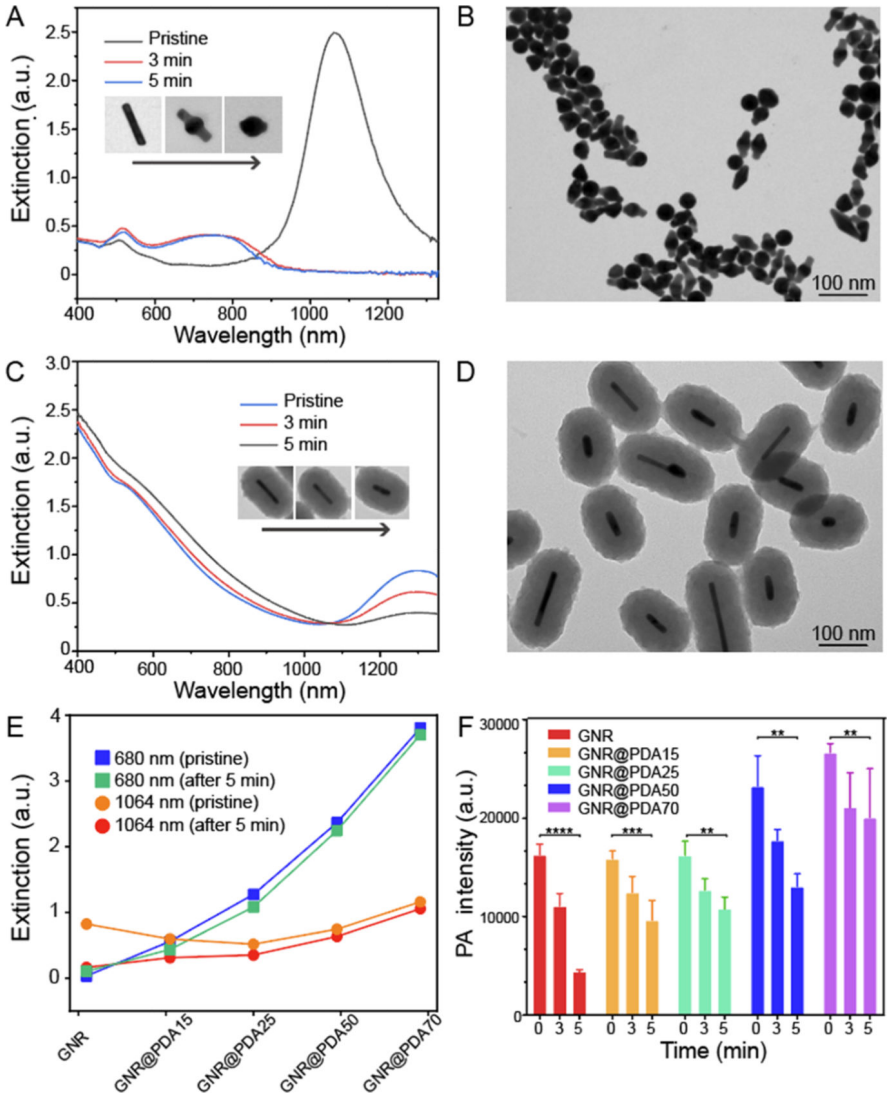

Figure 4.

GNR@PDA stability test. (A) Changes in optical extinction of GNRs before (blue line) and after 3 min (red line) and 5 min (gray line) of laser illumination. Inset images show the shape transition of the single GNR nanoparticle. (B) Morphology of GNRs was deformed after 5 min of laser illumination. (C) Changes in optical extinction of GNR@PDA50 before (blue line) and after 3 min (red line) and 5 min (gray line) of laser illumination. Inset images indicate that PDA coating protects GNR from the shape transition, retaining their rod-like structure. (D) Morphology of GNR@PDA50 after 5 min of laser illumination. (E) Changes in optical extinction at 680 and 1064 nm of GNR and GNR@PDAs before and after the laser illumination. (F) Time-dependent PA intensity of GNR and GNR@PDAs. We used 1064 nm laser for PA measurements. The error bars represent the standard deviations of five regions of interest. The statistical significance was calculated with the PA intensity of GNR@PDA's *t*-test; **, ***, and **** indicate $p < 0.01$, 0.001, and 0.0001 *vs* the pristine condition, respectively.

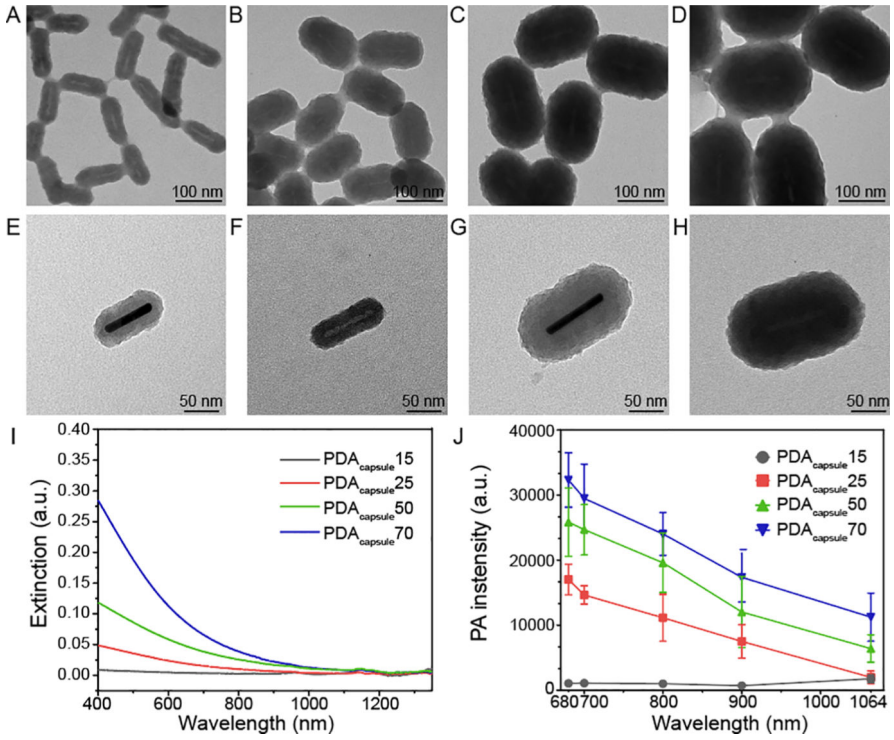

Figure 5.

PA performance of rod-shaped PDA capsules. TEM images of (A) $PDA_{capsule}15$, (B) $PDA_{capsule}25$, (C) $PDA_{capsule}50$, and (D) $PDA_{capsule}70$. TEM images of the single nanoparticle with high magnification: (E) GNR@PDA15, (F) $PDA_{capsule}15$, (G) GNR@PDA50, and (H) $PDA_{capsule}50$. Single nanoparticles with PDA thicknesses of 25 and 70 nm are shown in Figure S12. (I) UV–vis–NIR absorption spectra of PDA capsules. PDA capsules showed a similar extinction spectrum (*e.g.*, broadband absorption) like PDA nanoparticles.[49] (J) PA intensity of PDA capsules at 680, 700, 800, 900, and 1064 nm. The error bars represent standard deviation of five regions of interest.

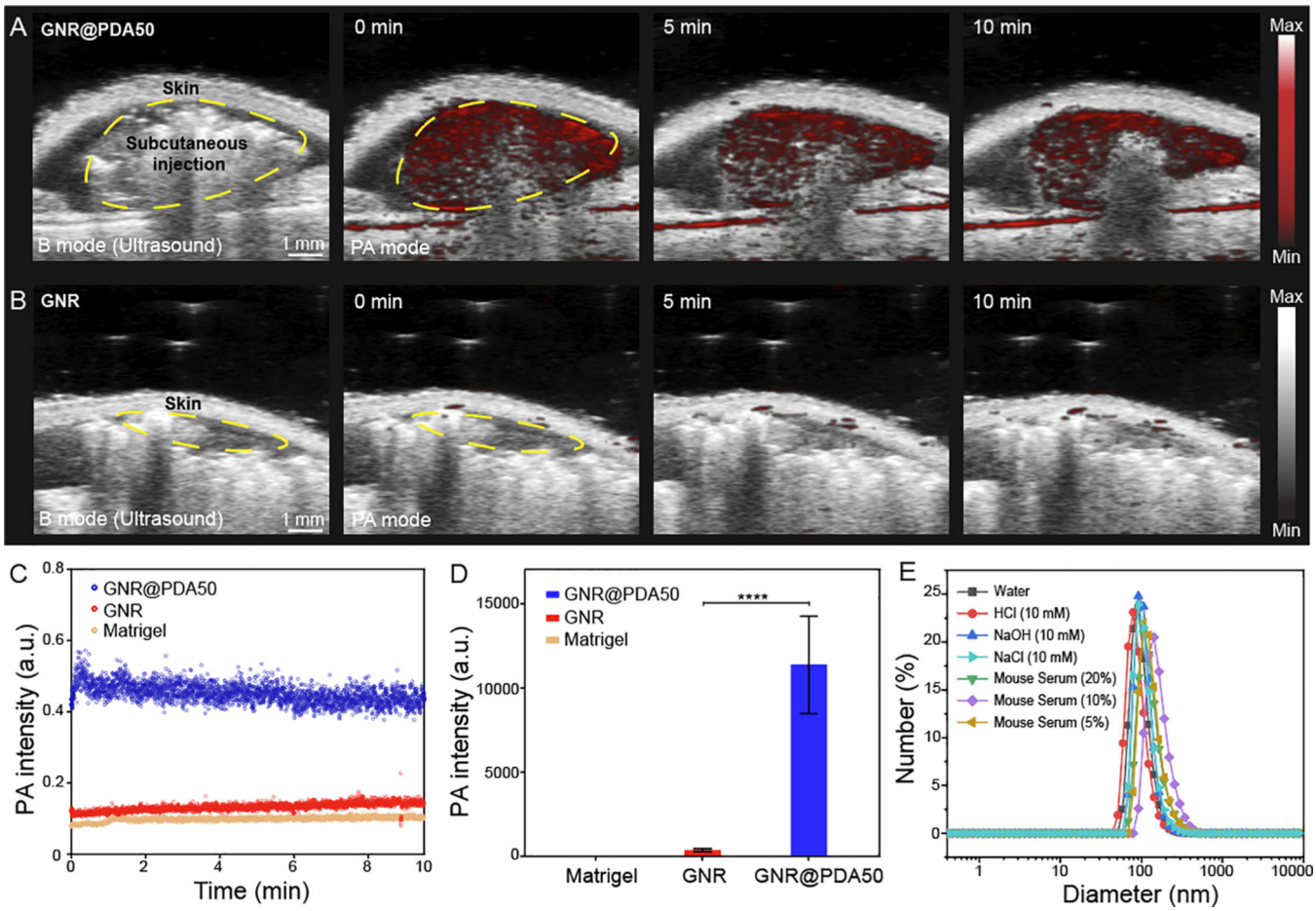

Figure 6.

PA imaging of GNR@PDA *in vivo*. B-mode ultrasound (gray scale) and PA (red scale) images of subcutaneously injected (A) GNR@PDA50 and (B) GNR, showing that GNR@PDA50 had higher PA intensity and signal stability than GNR. The same amount of GNR or GNR@PDA50 was injected into the mice ($n = 3$) based on a gold mass concentration of 0.2 μg/mL. PA signals of GNR and GNR@PDA50 were continuously measured in one spot for 10 min. The yellow circle is the subcutaneously injected area. (C) Time-dependent *in vivo* PA intensity of different materials. Blue, red, and orange circles indicate GNR@PDA50, GNR, and Matrigel, respectively. (D) Quantification of the PA signal comparing GNR and PDA@GNR50 at 0 min. The statistical significance was calculated with PA intensity of the GNR and GNR@PDA *via* a *t*-test; ****, $p < 0.0001$. Error bars represent three regions of interest. (E) GNR@PDA50 was incubated in different media for 1 h. DLS data showed that GNR@PDA was highly stable under different biological conditions.

Table 1.

Material Information of GNR and GNR@PDA Nanohybrids[a]

	diameter (*D*, nm)	length (*L*, nm)	volume (*V*, nm^3)	PDA thickness (nm)	mean aspect ratio
GNR	12.46 ± 1.36	95.07 ± 6.92	11,666.1 ± 2468.7	0	7.73 ± 1.10 (rods)
GNR@PDA15	43.34 ± 2.77	108.7 ± 9.25	160,916 ± 24,781.3	15.37 ± 1.08	
GNR@PDA25	64.58 ± 4.76	131.35 ± 8.96	432,813 ± 72,065.3	25.06 ± 1.95	
GNR@PDA50	117.41 ± 5.89	169.76 ± 8.27	1,839,200 ± 187,736	52.65 ± 3.82	
GNR@PDA70	155.25 ± 7.95	215.24 ± 9.99	4,088,595 ± 523,600	73.23 ± 3.99	

[a]Average diameter, length, volume, PDA thickness, and mean aspect ratio were calculated from 15 measurements.